



CHALMERS
UNIVERSITY OF TECHNOLOGY

Performance of magnetite fines for continuous hydrogen production

Downloaded from: <https://research.chalmers.se>, 2025-06-14 02:04 UTC

Citation for the original published paper (version of record):

Stanicic, I., Faust, R., Knutsson, P. et al (2025). Performance of magnetite fines for continuous hydrogen production. *International Journal of Hydrogen Energy*, 139: 753-765.
<http://dx.doi.org/10.1016/j.ijhydene.2025.05.223>

N.B. When citing this work, cite the original published paper.



Performance of magnetite fines for continuous hydrogen production

Ivana Staničić^{a,*}, Robin Faust^b, Pavleta Knutsson^b, Victor Purnomo^a, Henrik Leion^b, Tobias Mattisson^a, Magnus Rydén^a

^a Department of Space, Earth and Environment, Division of Energy Technology, Chalmers University of Technology, SE-412 58, Gothenburg, Sweden

^b Department of Chemistry and Chemical Engineering, Division of Energy and Materials, Chalmers University of Technology, Göteborg, 412 58, Sweden

ARTICLE INFO

Keywords:

Iron oxide
Steam-iron reaction
Hydrogen
Chemical looping water splitting

ABSTRACT

Hydrogen production from biogenic fuels in fluidized beds may provide the steel industry with a path to decarbonization and negative emissions. Magnetite fines (MAF), a common intermediate product in the European iron and steel industry, was utilized as an oxygen carrier for continuous hydrogen production. Performance was evaluated in a fluidized bed reactor, demonstrating that MAF effectively converts low-grade gaseous biofuels and subsequently generates high-purity hydrogen through water splitting. A kinetic model accounting for thermodynamic limitations was developed to assess MAF's reactivity towards reduction with CO and H₂, and oxidation with H₂O. The activation energy as a function of the mass conversion degree ranged from 32.7 to 70.5 kJ/mol for reduction with CO, and from 22.6 to 67.4 kJ/mol for H₂; for oxidation with H₂O, it ranged from 51.2 to 121.3 kJ/mol. Significant variations in the apparent activation energy were observed, which can be linked to changes in the rate-controlling mechanisms, highlighting the influence of microstructural evolution on reactivity. The findings provide valuable insights into the apparent kinetics of MAF and suitable operating conditions for optimizing hydrogen production, with the highest hydrogen production rate of 0.37 mmol g⁻¹ min⁻¹ achieved at 800 °C.

Nomenclature

AR	Air reactor	
CLWS	Chemical looping water splitting	
E _a	Activation energy	[kJ mol ⁻¹]
FR	Fuel reactor	
γ _i	Gas yield of component i	
γ _{i,eq}	Equilibrium gas yield of component i	
i	Gaseous components (CO, H ₂ , H ₂ O)	
k ₀	Pre-exponential factor	[s ⁻¹]
k _{F,i}	Apparent rate constant for component i	[m ³ kg ⁻¹ s ⁻¹]
K _{eq,Y,i}	Equilibrium constant for reaction Y and component i	
MAF	Magnetite fines	
m _{ox}	Mass of oxygen carrier in its oxidized state	[g]
M _O	Molar mass of oxygen	[kg kmol ⁻¹]
\dot{n}	Molar flow	[mol s ⁻¹]
p _i	Partial pressure of component i	[Bar]
SR	Steam reactor	
T	Temperature	[K]
$\dot{V}_{i,in}$	Inlet volumetric flow of component i	[m ³ s ⁻¹]
ω	Mass conversion degree	[-]

1. Introduction

Hydrogen and hydrogen-based fuels can play a fundamental role in sectors where emissions are hard to abate, and other mitigation measures are not available or difficult to implement [1]. However, today fossil fuel technologies dominate the global production of hydrogen [2]. According to the International Energy Agency, 70 % of the energy requirement for dedicated hydrogen production was met with light hydrocarbons, such as natural gas or naphtha, and the rest with coal in 2022. Considering the increasing global hydrogen demand, there is a need for rapid scale-up of hydrogen from other sources. For hydrogen to be a feasible future energy carrier, it needs to be produced in an economically viable manner and without CO₂ emissions. While electrolysis powered by renewable electricity is likely to become important in the future, other possibilities should be examined as well, including technologies that can achieve a combination of hydrogen production while simultaneously achieving negative CO₂ emissions.

One such alternative is the steam-iron process, which is one of the oldest methods to produce hydrogen [3]. The main advantage of the steam-iron process is the possibility of producing pure hydrogen without

* Corresponding author.

E-mail address: stanicic@chalmers.se (I. Staničić).

<https://doi.org/10.1016/j.ijhydene.2025.05.223>

Received 16 January 2025; Received in revised form 21 April 2025; Accepted 16 May 2025

Available online 27 May 2025

0360-3199/© 2025 The Authors. Published by Elsevier Ltd on behalf of Hydrogen Energy Publications LLC. This is an open access article under the CC BY license (<http://creativecommons.org/licenses/by/4.0/>).

further gas-cleaning steps, while simultaneously producing a concentrated CO₂ stream that can be used for carbon capture and storage (CCS). This is of particular importance when using biomass as a feedstock, where a normal gasification process would entail significant gas cleaning and handling of impurities and higher hydrocarbons, or tars.

At the core of this process is the steam-iron reaction (SIR), where reduced iron oxides are oxidized with steam to produce pure hydrogen. It is a stepwise process where each reaction step releases or requires heat, and the kinetics and thermodynamics of each of the steps are strongly dependent on the temperature [4]. Thus, the reactions are preferably conducted at different temperature levels, making the original batch process cumbersome and inefficient. However, it is possible to realize a continuous process, for example by applying a system with interconnected fluidized beds [5–7]. Such a system with three interconnected reactors, referred to as Chemical Looping Water Splitting (CLWS) or Chemical Looping Hydrogen Production (CLH), is illustrated in Fig. 1.

1.1. Steam-iron reaction

The continuous process is realized using three interconnected reactors, referred to as the fuel reactor (FR), steam reactor (SR), and air reactor (AR) as illustrated in Fig. 1.

In the fuel reactor, hematite (Fe₂O₃) is reduced to magnetite (Fe₃O₄), wüstite, and potentially to metallic iron (Fe). For the purposes of simplicity, wüstite is referred to as stoichiometric FeO, although non-stoichiometric variations do exist under these conditions. The reactions using CO as model fuel are illustrated in (1–3). Reduction to metallic iron is often avoided in fluidized beds as it has been observed to cause sintering and consequently defluidization of the bed [8]. Although all kinds of hydrocarbon fuels can be utilized in this process, bio-based fuels are expected to be favored in the future, since they offer the potential to achieve negative emissions through Bio-Energy Carbon Capture and Storage (BECCS). Furthermore, from a practical standpoint, reactor design would be more straightforward for gaseous fuels compared to solid fuels, making gasified biomass and pyrolysis gas an

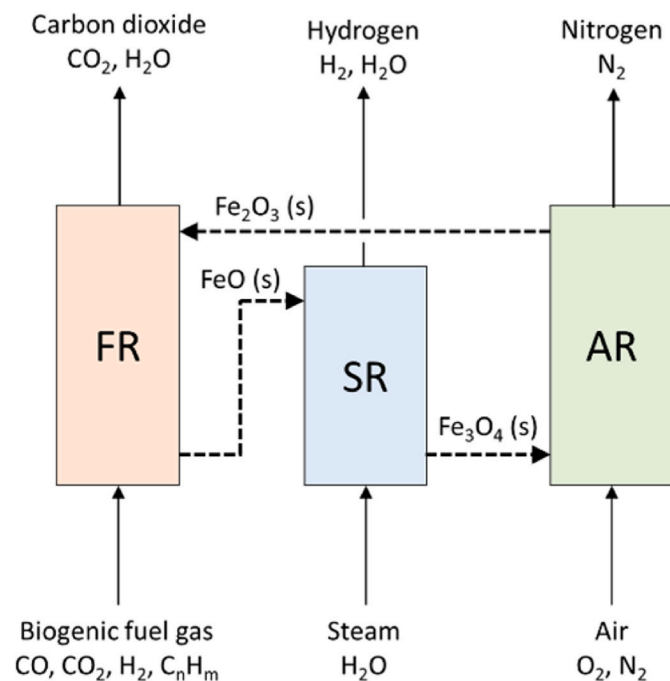


Fig. 1. Schematic description of Chemical Looping Water Splitting (CLWS) for continuous production of hydrogen through the steam iron reaction. The process consists of three interconnected fluidized bed reactors, fuel reactor (FR), steam reactor (SR), and air reactor (AR).

excellent starting point. When the fuel is oxidized, the iron oxide is reduced until equilibrium is reached. However, complete gas conversion is not possible for reactions 2 and 3 in conventional fluidized beds, see Fig. 2. Consequently, unreacted H₂ and CO will be present in the exiting flue gas. To overcome this limitation, one solution is to perform the reduction in a counter-current flow setup, e.g. counter-current moving bed [9] or packed fluidized bed [10]. With a counter-current flow setup, complete gaseous conversion can be achieved, facilitating the separation of CO₂ from the flue gas stream.



In the steam reactor, H₂ is produced by oxidizing FeO, and possibly Fe, with steam according to reactions 4 and 5. The outgoing gas contains a mixture of steam and hydrogen, but a pure H₂ stream can be obtained easily by condensing the steam. Due to thermodynamic limitations, the iron oxide can only be oxidized to magnetite in the steam reactor.



Lastly, regeneration occurs in the air reactor where the metal oxide is completely oxidized according to reaction 6.



The hydrogen yield at different temperatures under equilibrium conditions for the various iron oxides and metallic iron is presented in Fig. 2. The reduction of Fe₂O₃ proceeds stepwise through magnetite, wüstite and finally to metallic iron. These equilibria, along with the associated reaction enthalpies in reactions (1–6), were calculated using FactSage 8.3 [11]. As seen in Fig. 2, lower temperatures favor higher hydrogen yields thermodynamically. However, in practice, lower temperatures also lead to reduced reaction rates. Therefore, within the steam reactor, there is a trade-off between kinetic and thermodynamic limitations that must be carefully considered for optimal hydrogen production.

1.2. Kinetics of iron oxides in fluidized beds

Reduction and oxidation kinetics are important for predicting the rate at which the reaction proceeds. It does not only provide physical insights into the reactions but is also an important tool for scale-up and defining reactor dimensions and energy consumption. In general, the reduction rate in fluidized beds is limited by mass transfer through the external gas film to the solid surface, diffusion in the porous or dense product layer, interfacial phase reaction or a combination of several mechanisms. Further, the kinetic parameters largely depend on the material (type, shape, composition and impurities), the reducing gas (composition and impurities) but also the temperature and type of experiment.

Most prior studies on the steam-iron reaction have been conducted in small, fixed beds or by TGA. There are a few studies where the apparent kinetics of iron materials have been determined in fluidized beds, but these have usually focused on the reduction step or oxidation with steam at lower temperatures (<600 °C) [12,13]. A summary of kinetic parameters for the reduction and oxidation of iron oxides under relevant conditions for the steam-iron-reaction is summarized in Table 1.

While there have been extensive studies on iron reduction mechanisms in TGA, there are different aspects to consider in fluidized beds. For example, reduction to metallic Fe in fluidized beds is often seen as problematic due to sintering of the material, which leads to a decrease in the H₂-yield [8]. For that reason, literature on kinetic data for reduction

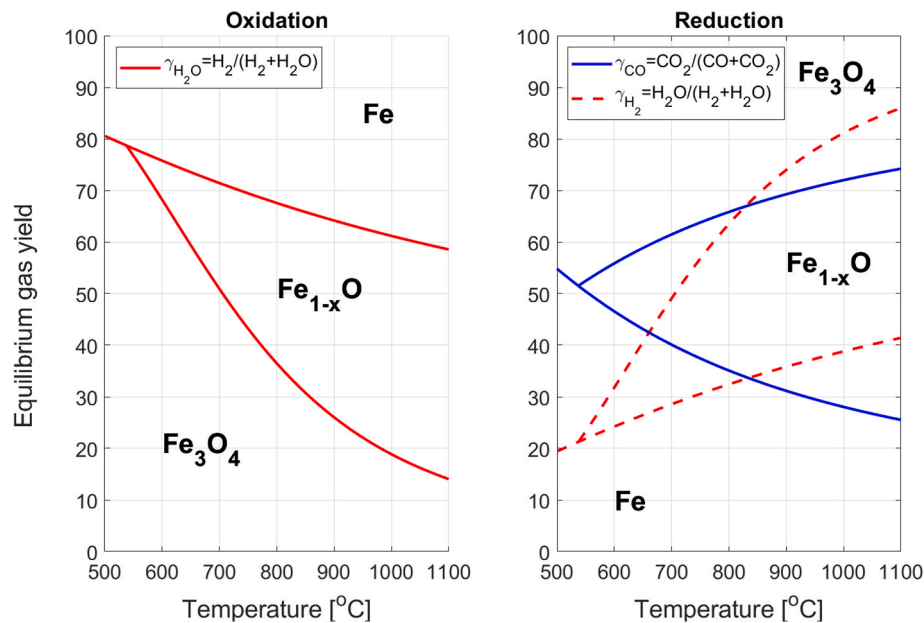


Fig. 2. The equilibrium gas yields during oxidation and reduction of iron oxides. The figure illustrates the gas yield at equilibrium for different process temperatures.

Table 1

Summary of kinetic parameters reported in literature for the reduction and oxidation of iron oxides relevant for the steam-iron reaction.

Experimental Setup	Material	Fuel Gas	Reaction(s)	Activation Energies (kJ/mol)	Temp (°C)	Ref
Fluidized bed	Iron ore (250–350 μm)	Mixtures of H ₂ , N ₂ and H ₂ O	Reduction to Fe	-	600–800	[14]
Micro fluidized bed	Fe ₂ O ₃ (60.7 μm)	CO	Fe ₂ O ₃ → Fe ₃ O ₄ Fe ₃ O ₄ → FeO	30.6–52.99 52.44–80.83	750–950	[15]
Micro fluidized bed	Brazilian iron ore (100–150 μm)	50 % CO in N ₂	FeO → Fe Fe ₂ O ₃ → Fe ₃ O ₄ Fe ₃ O ₄ → FeO	45.74–92.12 29.1 40.9	700–850	[16]
Fluidized bed	Iron ore (106–150 μm)	H ₂	–	–	600–800	[17]
Fluidized bed	Hematite ore (45–88 μm)	H ₂	Fe ₂ O ₃ → Fe	23.8–54.9	700–850	[18]
Fluidized bed	Boron-bearing iron concentrate	H ₂	Early reduction Late reduction	65.2 96.1	650–850	[19]
In-situ high temperature hot stage and microscopy	Hematite (80–88 μm)	CO	Fe ₂ O ₃ → Fe ₃ O ₄ Fe ₃ O ₄ → FeO FeO → Fe	50.0 40.3 47.1	700–1100	[20]
TGA	Dense Fe ₂ O ₃ briquettes (200 μm)	CO	Fe ₂ O ₃ → Fe ₃ O ₄ Fe ₃ O ₄ → FeO	56.5 22.1	700–1050	[21]
TGA	Iron ore (90–200 μm)	H ₂	Fe ₂ O ₃ → Fe ₃ O ₄ Fe ₃ O ₄ → FeO	28.7 168.6	700–1050	[22]
TGA	Synthetic particles (100–300 μm)	H ₂	Fe ₂ O ₃ → Fe	83	700–850	[22]
TGA	Synthetic particles (100–300 μm)	O ₂	Fe → Fe ₂ O ₃	30	500–850	[23]
TGA	Synthetic particles (100–300 μm)	CH ₄	Fe ₂ O ₃ → Fe	–	950	[23]
Monolithic reactor	Iron rod	H ₂ O in N ₂ and Ar	Fe → Fe ₃ O ₄	47	400–600	[24]
TGA	Hematite (125 μm)	H ₂ O	FeO → Fe ₃ O ₄	77.9	500–900	[25]

to metallic iron or wüstite in fluidized beds at temperatures above 850 °C is scarce. Most investigated iron-based materials have been ores, which can contain a significant fraction of impurities such as Si, Ca, Mg, etc. These impurities could have an influence on the reduction mechanism, sintering behavior and/or the overall reactivity of the material [26]. For example, studies have demonstrated that alkaline earth metal oxides can prevent sintering and thereby improve stability during reduction [27], showing that impurities can impact the performance of iron-based materials.

Kinetic studies on the oxidation of metals and metal oxides with steam in fluidized beds remain limited. However, parallels can be drawn

to the oxidation reaction with air in chemical looping combustion. Oxidation with steam has been reported to follow a similar product-layer mechanism to that observed with air however, it is anticipated that significantly higher activation energies would be required for steam oxidation [25]. This is exemplified by two studies reporting the activation energy to be 77.9 kJ/mol for steam oxidation of iron oxides [25], whereas the activation energy for oxidation with air is much lower, 30 kJ/mol [22]. Despite these findings, only a few studies have investigated the kinetics of reduction and oxidation of iron oxides in fluidized bed experiments for hydrogen production [12]. There is a clear knowledge gap in literature, not only concerning the deep reduction of iron oxides

in fluidized beds, but also in understanding the kinetics of oxidation with steam.

1.3. Aim of study

The main objective of this study is to examine the performance of iron oxide particles for the continuous production of hydrogen in fluidized beds. The selected oxygen carrier is an iron oxide called magnetite fines (MAF) and is a particulate intermediate product in the European iron and steel industry that is available in huge amounts. Such materials may have great potential for the steam-iron reaction but have not been investigated in literature previously. Utilizing MAF for continuous hydrogen production presents an interesting option for the European steel industry to achieve fossil-free steel production. With several European countries setting goals to replace fossil fuels with hydrogen in the steel industry, the potential application of MAF in steam-iron reaction becomes even more significant to investigate. This process does not only enable hydrogen production, but also contributes to achieving negative emissions, advancing the decarbonization of steel production, and supporting the goal of sustainable steel manufacturing.

This study addresses the knowledge gap regarding the utilization of MAF as an oxygen carrier for hydrogen production. Feasible operating parameters are investigated to maximize the production of hydrogen during extensive reduction of iron oxides in fluidized beds. Given the scarcity of kinetic data derived from fluidized bed experiments, the aim is to extract apparent kinetic data under realistic operating conditions. A kinetic model is developed that takes thermodynamic limitations into account and is implemented to study the reactivity of iron oxide with the key components: H₂, CO and H₂O. This study is confined to a simplified system utilizing the two key fuel components, CO and H₂. Although biomass-derived fuel gases from gasification or pyrolysis could contain additional hydrocarbons, tars, sulfur compounds, and other contaminants, the effect of these impurities is beyond the scope in this study. Still, it is expected that the study will have significant implications also for use with solid fuels, as oxygen carriers are expected to react primarily with gaseous components.

2. Material and method

Magnetite Fines (MAF) is an enriched iron ore product produced by LKAB and primarily used in sintering processes to form pellets, which are subsequently smelted into iron in the blast furnace. MAF serves as a key intermediate product in the iron and steel industry, and it is a mechanically beneficiated iron ore product containing over 98 wt% iron oxides (see Table 2). Its high iron content makes MAF particularly interesting for the steam-iron reaction. Previous studies have investigated MAF's potential for chemical looping combustion and oxygen carrier aided combustion, showing favorable reactivity under fluidized bed conditions [28].

Prior to the experiments, MAF was calcined at 950 °C for 12 h in air. After calcination, the material was sieved to obtain particle sizes ranging from 90 to 180 μm.

2.1. Experimental setup

Experiments were conducted in a quartz fluidized bed batch reactor mounted inside an electrically heated furnace. The height and the inner diameter of the reactor were 820 mm and 22 mm, respectively. A porous quartz plate placed 380 mm from the bottom of the reactor kept the bed material in the reactor, while allowing the through-flow of gas to

fluidize the bed. The pressure fluctuations over the reactor were monitored using a pressure sensor (Honeywell pressure transducer, 20 Hz). The temperature in the bed and under the porous plate was monitored using two K-type thermocouples as illustrated in Fig. 3.

The gas entering the reactor was regulated by four magnetic valves as shown in Fig. 3. The total flow to the reactor varied between 800 and 1200 ml/min. At these flow rates, the bed was a bubbling bed with $U/U_{mf} \sim 3.5\text{--}4.2$, where U is the superficial gas velocity and U_{mf} is the minimum fluidization velocity calculated according to Wen and Yu [29] correlation. Steam was generated by injection of Milli-Q water into a controlled evaporation mixing (CEM) system heated to 150 °C and was mixed with N₂. To prevent condensation of steam, the streams to and from the reactor were electrically heated to temperatures between 115 °C and 150 °C.

The gas exiting the reactor was cooled in an M&C ECP1000 condenser to ensure that no water entered the dry gas analyzer. The dry gas analyzer (Rosemount NGA 2000) was equipped with IR/UV sensors for CH₄, CO₂, and CO, a thermal conductivity sensor for H₂, and paramagnetic gas sensor for O₂. The volumetric flow rate and concentrations (CO₂, CO, CH₄, H₂, and O₂) were monitored with a frequency of 1 Hz. The concentration was measured using a non-dispersive infrared (NDIR) analyzer. The analyzer was calibrated for the range of 0 %–40 % CO₂, 20 % CO, 25 % CH₄, 15 % H₂ and 5 % O₂.

Before the start of each experiment, the top and bottom parts of the reactor were tightly sealed to avoid leakage and to ensure this, a leak test was performed. Then, the reactor was heated under oxidizing conditions, denoted as AR. Once the desired temperature was reached, the gas was switched to nitrogen to purge the reactor and avoid mixing between fuel and steam or air. For the reduction, denoted as FR, a mixture of syngas (50 % CO + 50 % H₂), or CO, in nitrogen was used. The reduction was followed by a purging step before the hydrogen production step, denoted SR. Details about the experimental parameters used for one experimental cycle are given in Table 3.

Each experiment was preceded by ten cycles that excluded the steam reactor (SR) step 5. These initial cycles are hence referred to as *activation*. Following activation, two sets of experiments were conducted (steps 3.1 and 3.2 in Table 3). The first set of experiments focused on investigating the performance of MAF during consecutive cycling, but also suitable parameters for steam reactor such as temperature and reduction level. For this purpose, 15 g of material was used with CO or syngas. The reduction step was always conducted at 900 °C, and the desired temperature in the steam oxidation step was achieved during the inert step. Oxidized bed samples were extracted after step 5 and 29 cycles, and at the end of the experiment after step 1 and 53 cycles. In the follow-up experiment, syngas was used to study the particles after activation, and after the last cycle and step 3.1. The second set of experiments focused on obtaining key kinetic parameters in the FR. Therefore, syngas was used along with 2.5 g of MAF mixed with 8.5 g silica sand to investigate the reactivity towards CO and H₂. The temperature varied in 25 °C steps from 850 to 975 °C. The reactor was cooled down in an inert atmosphere before the samples were extracted.

2.2. Data analysis

The weight loss of the OC during experiments can be measured by the solid mass conversion degree (ω) described as:

$$\omega(t) = \frac{m(t)}{m_{ox}} \quad 7$$

Table 2

Composition of magnetite fines MAF (wt. %), according to product specifications. Reported as oxides.

Fe ₃ O ₄	SiO ₂	K ₂ O	Al ₂ O ₃	CaO	MgO	MnO	TiO ₂	V ₂ O ₅	P ₂ O ₅
98.11	0.7	0.02	0.3	0.2	0.3	0.05	0.3	0.3	0.01

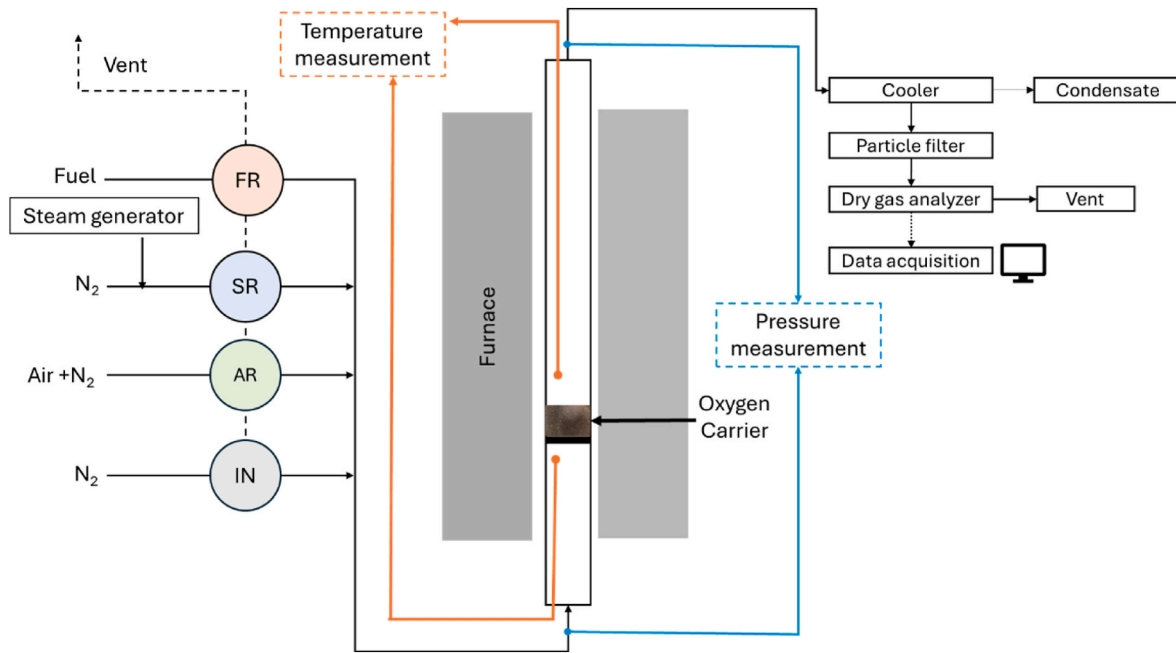


Fig. 3. Schematic overview of the fluidized bed batch reactor setup.

Table 3
Experimental parameters used for one experimental cycle.

Step	Cycle	Time [s]	Total flow [NmL/min]	Gas composition	T [°C]
1	Oxidation (AR)	Until O ₂ = 5.3 %	1200	5.3 % O ₂ 94.7 % N ₂	900
2	Inert (SR)	180	1200	100 % N ₂	
3.1	Reduction (FR)	60–350	1200	45 % CO or syngas 55 % N ₂	900
3.2	Reduction (FR)	120	800	43.75 % syngas 56.25 % N ₂	850, 875, 900, 925, 950, 975
4	Inert	180	1200	100 % N ₂	
5	Steam (SR)	Until H ₂ < 0.1 %	1100	54.5 % H ₂ O 45.5 % N ₂	600, 700, 800, 900
6	Inert	180	1200	100 % N ₂	

In theory, the transition between phases occurs at specific ω -values, corresponding to distinct oxidation states of the material. Table 4 summarizes the transitions between these phases, with Fe₂O₃ being the most oxidized form, and Fe the most reduced form.

During reduction, the mass conversion degree (ω) as a function of time can be calculated from the outlet gas concentrations and the molar gas flows of dry gases. For syngas, that is:

$$\begin{aligned} \omega(t) &= \omega(t-1) - \frac{M_{\text{O}}}{m_{\text{ox}}} \int_{t-1}^t \dot{n}_{\text{dry}}(t)(x_{\text{CO}_2}(t) + x_{\text{H}_2\text{O}}(t)) dt \\ &= \omega(t-1) - \frac{M_{\text{O}}}{m_{\text{ox}}} \int_{t-1}^t \dot{n}_{\text{dry}}(t)(2x_{\text{CO}_2}(t) + x_{\text{CO}}(t) - x_{\text{H}_2}(t)) dt \end{aligned} \quad 8$$

In Equation 8, the net oxygen removal from the oxygen carrier is derived from elemental carbon and hydrogen balances, accounting for the total oxygen incorporated into the oxidized products CO₂ and H₂O. Since H₂O is not directly measured, its amount is derived based on the known equimolar composition of CO and H₂ in the fuel, i.e., $x_{\text{H}_2\text{O}} = x_{\text{CO}_2} + x_{\text{CO}} - x_{\text{H}_2}$. Thus, oxygen removal is expressed as $x_{\text{CO}_2} + x_{\text{H}_2\text{O}}$, which after substituting for $x_{\text{H}_2\text{O}}$, leads to the final expression: $2x_{\text{CO}_2} + x_{\text{CO}} - x_{\text{H}_2}$. The conversion of the oxygen carrier as a function of time in the steam and air reactors are defined as:

$$\omega(t) = \omega(t-1) + \frac{M_{\text{O}}}{m_{\text{ox}}} \int_{t-1}^t \dot{n}_{\text{dry}}(t)(x_{\text{H}_2}(t)) dt \quad 9$$

$$\omega(t) = \omega(t-1) + \frac{M_{\text{O}}}{m_{\text{ox}}} \int_{t-1}^t \dot{n}_{\text{dry}}(t)(x_{\text{O}_2,\text{in}}(t) - x_{\text{O}_2,\text{out}}(t)) dt \quad 10$$

The extent of fuel conversion can be described by the gas yield, which is calculated from the measured gas concentrations. For example, the gas yield of the gaseous component CO is defined as:

$$\gamma_{\text{CO}} = \frac{\dot{n}_{\text{CO}_2}}{\dot{n}_{\text{CO}} + \dot{n}_{\text{CO}_2}} \quad 11$$

For the conversion in steam reactor, data obtained from the gas analyzers is recalculated to a wet basis using the flow of the carrier gas (N₂) and the dry concentration of hydrogen. Then, the hydrogen yield is obtained from:

$$\gamma_{\text{H}_2} = \frac{\dot{n}_{\text{H}_2}}{\dot{n}_{\text{H}_2} + \dot{n}_{\text{H}_2\text{O}}} \quad 12$$

To evaluate the potential of the oxygen carrier, the hydrogen production rate R_{H_2} (mmol g⁻¹ s⁻¹) was calculated according to the

Table 4
Theoretical transition values between different iron phases for the mass conversion degree (ω).

Reaction	ω -transition values [–]
6 Fe ₂ O ₃ → 4 Fe ₃ O ₄ + O ₂	$\omega_1 = 0.967$
2 Fe ₂ O ₃ → 4 FeO + O ₂	$\omega_2 = 0.900$
2 Fe ₂ O ₃ → 4 Fe + 3 O ₂	$\omega_3 = 0.700$

following:

$$R_{H_2} = \frac{\int_t^{t+\Delta t} \dot{n}_{dry}(t)(x_{H_2}(t))dt}{22.4 \Delta t m_{ox}} \quad 13$$

2.2.1. Kinetic model

As evident from equilibrium, Fig. 2, distinct limitations exist for reactions (2) to (5). The kinetic expressions derived here will therefore account for thermodynamic limitations by considering the equilibrium partial pressure ($p_{i,eq}$) of component i . Starting from a mass balance over a partial mass element (dm) of the bed, the difference in partial pressure of component i can be written as:

$$\frac{\partial p_i}{\partial m} = -\frac{k_{F,i}}{\dot{V}_{i,in}} (p_i - p_{i,eq}) \quad 14$$

Where $\dot{V}_{i,in}$ is the volumetric flow of component i (either CO, H₂ or H₂O). Here, the apparent rate constant $k_{F,i}$ is a first-order mass-based and volume-normalized rate constant that indicates the reactivity of MAF, i . i . e. quantifies the ability to convert gaseous fuel components at certain temperatures and mass conversion degrees. There are different possible methods to obtain the apparent rate constant $k_{F,i}$, and the model proposed here is similar to that developed by Mei et al. [30] and Markström et al. [31]. The model presumes that the gas travels in plug-flow through a well-mixed bed of particles. However, in contrast to previous studies, this model also considers the thermodynamic driving force.

The differential equation (15) has an analytical solution which gives the partial pressure p_i of component i , at coordinate m . Assuming a first-order reaction for the consumption of the reactant i by the oxygen carrier gives:

$$p_i = p_{i,eq} + (p_{i,0} - p_{i,eq}) e^{-\frac{k_{F,i}m}{\dot{V}_{i,in}}} \quad 15$$

where m is the mass of oxygen carrier in kg and $p_{i,0}$ is the inlet partial pressure of component i . Consequently, the gas yield of component i can be described as:

$$\gamma_i = \gamma_{eq,Y,i} \left[1 - e^{-\frac{k_{F,i}m}{\dot{V}_{i,in}}} \right] \quad 16$$

where $\gamma_{eq,Y,i}$ is the equilibrium gas yield for component i and reaction Y defined as:

$$\gamma_{eq,Y,i} = \frac{K_{eq,Y,i}(T)}{1 + K_{eq,Y,i}(T)} \quad 17$$

The temperature-dependent expressions for the equilibrium constants $K_{eq,Y,i}(T)$ have been derived from FactSage 8.3 [11]. A summary of the equilibrium constants for different reactions is summarized in Table 5.

Consequently, the first-order apparent rate constant, with the unit $m^3 kg^{-1} s^{-1}$, can be derived from equations (11) and (17):

$$k_{F,i}(\omega, T) = -\frac{\dot{V}_{i,in}}{m_{ox}} \ln \left[1 - \frac{\gamma_i}{\gamma_{i,eq}} \right] \quad 18$$

With this approach, the apparent rate constant $k_{F,i}$ can be derived from the experimental measurements of the gas yields. However, at low hydrogen concentrations, the gas analyzer can provide inaccurate readings due to interference from other gaseous components. To address this issue, the apparent rate constant for the yield of hydrogen in the fuel reactor was calculated using a correction factor, δ , using the same approach as in previous work [30]. This factor accounts for the molar ratio of the total oxygen consumed by hydrogen and CO.

Table 5

The temperature-dependent expression for the equilibrium constants $K_{eq,Y,i}(T)$ as a function of ω . Temperatures are given in Kelvin. Expressions for reactions 1 and 2 were derived between 973 and 1473 K, while 4 was derived between 873 and 1273 K.

Reaction, component	$K_{eq}(T)$ [-]	ω range [-]
1, CO	$K_{eq,1,CO} = e^{\left(\frac{-4636.4}{T+6.0178}\right)}$	$\omega > 96.7$
1, H ₂	$K_{eq,1,H_2} = e^{\left(\frac{669.06.4}{T+9.6174}\right)}$	
2, CO	$K_{eq,2,CO} = e^{\left(\frac{-1969.1}{T+2.491}\right)}$	$90.0 < \omega < 96.7$
2, H ₂	$K_{eq,2,H_2} = e^{\left(\frac{-5930.6}{T+6.0852}\right)}$	
4, H ₂ O	$K_{eq,4,H_2O} = e^{\left(\frac{6171.2}{T-6.3054}\right)}$	

$$\delta = \frac{\dot{n}_{H_2,in} - \dot{n}_{H_2,out}}{\dot{n}_{CO,in} - \dot{n}_{CO,out}} \quad 20$$

As the reduction progresses, the value of δ varies between 1.0 and 1.4, and these variations are accounted for in the derivation of the rate constant for hydrogen.

$$k_{F,H_2} = \delta k_{F,CO} \quad 21$$

After obtaining the mass-based rate constants, as a function of the mass conversion degree and temperature using experimental data, the activation energy and pre-exponential factor were determined using the Arrhenius equation, shown in equation (23):

$$k_{F,i}(\omega, T) = k_0 e^{-\frac{E_a}{R T}} \quad 23$$

Here, T is the absolute temperature in Kelvin, R is the universal gas constant, E_a is the apparent activation energy, and k_0 is the pre-exponential factor.

The magnitude of the activation energy can provide valuable insights into the underlying rate-controlling mechanisms for the reduction of iron oxides. As summarized by Strangway [32], the correlation between activation energy values and specific rate-controlling steps is as follows: values within 8–16 kJ/mol are indicative of gas diffusion control, 29–42 kJ/mol correspond to a combination of gas diffusion and interfacial chemical reactions, 60–67 kJ/mol suggest interfacial chemical reaction control, and values exceeding 90 kJ/mol point towards solid-state diffusion control. Although these ranges are not absolute, they provide a recognized framework for identifying probable rate-controlling mechanisms [33,34].

While a simple kinetic law has been applied in this study, more complex kinetic models could certainly be considered. However, the aim of this work is not to identify the most optimal kinetic model, but rather to investigate the kinetics and evaluate the applicability of the proposed model. Although the rate constant derived here does not offer intricate kinetic details, it still serves as a useful tool for assessing reactivity and can be utilized for reactor design and dimensioning purposes.

2.3. Material characterization

The chemical phases formed during the utilization of MAF were investigated with X-ray diffraction (XRD) with a Bruker D8 Discover diffractometer. MoK α radiation ($\lambda = 0.7107 \text{ \AA}$) was used to mitigate the fluorescence of the commonly used Cu K α radiation obtained when Fe is present in the sample. The particles were examined without any prior treatment (e.g., grinding). The obtained spectra were matched to the PDF 5+ database with the Diffrac EVA 7.0 software.

Scanning electron microscopy (SEM) was used for morphological analysis with a Quanta 200 ESEM FEG. The particles were mounted on

carbon tape for top-view images. Cross-sections were prepared by embedding the particles in epoxy resin and subsequently grinding and polishing them with SiC paper to obtain a surface quality suitable for SEM analysis. Both top-views and cross-sections were analyzed with back-scattered electrons signal (BSE). Information about the chemical composition of the particles was obtained from the X-rays generated through interaction of the electron beam with the sample, by so-called energy-dispersive X-ray spectroscopy (EDS).

3. Results and discussion

3.1. Impact of activation

Iron-based oxygen carriers often experience a change in reactivity when they are exposed to the first reduction and oxidation cycles. MAF exhibited a continuous increase in the rate of conversion during the initial cycles, as shown in Fig. 4. Here, the rate of reduction is shown in wt% per minute, as a function of the mass conversion degree (ω) during reduction with syngas. The duration of the reduction for the initial 14 cycles and the last six cycles were 70 s and 130 s, respectively. The rate stabilized at 2.2 wt% per minute, and it was shown that at least ten cycles are required before stable reactivity is achieved. Hence, the results presented in this paper are based on data obtained post-activation.

During activation, the particles undergo significant morphological changes, further addressed in Section 3.5. These transformations, including the formation of an iron rich-layer at the particle surface as well as formation of cracks and increase in porosity, contribute to enhanced performance and increased reactivity over successive cycles. The observations discussed here provide insights into the gradual improvement in reactivity and provide a foundation for understanding the results presented later in this study.

3.2. Gas concentration profiles

The gas concentration profiles provide valuable information into the reaction dynamics during each phase in the cycle. Fig. 5 presents the dry gas concentration profiles and the mass conversion degree during one cycle, for the reduction of MAF with syngas. The profiles are plotted as a function of reaction time, with the mass conversion degree shown on the secondary y-axis. Each cycle comprises three main phases - reduction (FR), steam oxidation (SR), and air oxidation (AR) - each followed by an inert step. The oxidation step (AR) is carried out until MAF reaches full oxidation, i.e. $\omega = 1$ (not shown in the figure due to truncation of the final, slower part of the reaction).

In the reduction phase (FR), the conversion of CO to CO₂ is observed to be the highest at the start of the reduction period, reflecting the high

reactivity and high gas yield. After 55 s, the CO₂-concentration begins to decline, while the concentrations of CO and H₂ increase. This shift occurs when the mass conversion degree value falls below 96.7 wt%, which indicates that the bed has been depleted of hematite and thus enters the area where magnetite and wüstite will be present and equilibrium constraints for fuel conversion are active. For reduction with magnetite, complete fuel conversion is not achievable as illustrated in Fig. 2.

Following the reduction phase, steam is introduced to oxidize the reduced iron oxides. During this step, the primary product is H₂, with trace amounts of CO and CO₂ detected at the beginning of the oxidation period. These transient peaks are most prominent during the initial few seconds of the steam oxidation step and are attributed to residual carbon species deposited on the particles during the prior reduction phase. To assess the potential impact of carbon deposition on hydrogen purity, a carbon release ratio (C/C_{tot}) was calculated comparing the amount of CO and CO₂ released during oxidation relative to the total carbon-containing gases fed during the reduction. The C/C_{tot} - value was always well below 0.75 %, as shown in Fig.A.1. These results indicate that carbon deposition is minimal under the investigated conditions and does not significantly affect the hydrogen quality.

3.3. Phase characterization

To explain the observed shift in equilibrium during reduction it is important to understand the correlation between the mass conversion degree (ω) and the crystalline phases. As shown in Fig. 5, the conversion indicates that the system undergoes a shift in equilibrium, particularly when the ω falls below 0.967. By analyzing the crystalline phases at different ω , a deeper understanding of how phase transformations influence the overall reaction can be gained. Therefore, crystalline phases at varying mass conversion degrees were examined using XRD. Samples were extracted following the reduction ($\omega = 0.928$) and steam oxidation ($\omega = 0.967$). The crystalline phases are presented in Fig. 6, showing the correlation between the mass conversion degree and the crystalline phases.

The analysis shows that calcined MAF predominantly consists of hematite. The sample extracted after the reduction phase shows a significant fraction of wüstite, mixed with magnetite. Following the steam oxidation phase, wüstite is no longer detected in the sample, indicating complete conversion to magnetite. This analysis aligns the observed chemical phases, with the expected phases at their theoretical transition values as outlined in Table 4. This correlation supports the explanation of the shift in equilibrium by correlating the mass conversion degree with crystalline phases.

3.4. Reactivity with gaseous fuels

While iron-based oxygen carriers can experience an increase in reactivity during the initial cycles, they can also exhibit a decrease in reactivity (deactivation) over time due to factors such as agglomeration or thermal sintering. Therefore, it is important to investigate how reactivity evolves both as a function of cycles and the extent of reduction.

Fig. 7a presents the gas conversion of CO, while Fig. 7b illustrates the rate of conversion after 20, and up to 51 cycles. Here, a clear decrease in both yield and rate of conversion below the mass conversion degree 0.967 is seen. This decrease is observed due to the thermodynamic limitation in the system due to the depletion of hematite and thus transition toward a new equilibrium state.

As observed in Fig. 4, the reactivity increases during the initial 10 cycles before stabilizing up to 40 cycles, after which a gradual decline is observed. This behavior indicates that the rate of conversion is also influenced by the total number of cycles. As observed in Fig. 7, the reduction time in cycle 51 was extended to reach the limit for pure wüstite and the transition to metallic iron ($\omega = 0.899$). However,

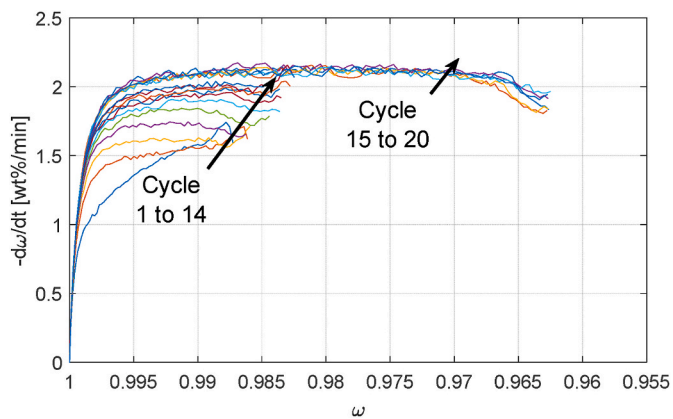


Fig. 4. The rate of conversion ($-d\omega/dt$) as a function of the mass conversion degree (ω) for the first 20 cycles during reduction of 15 g MAF with syngas at 850 °C.

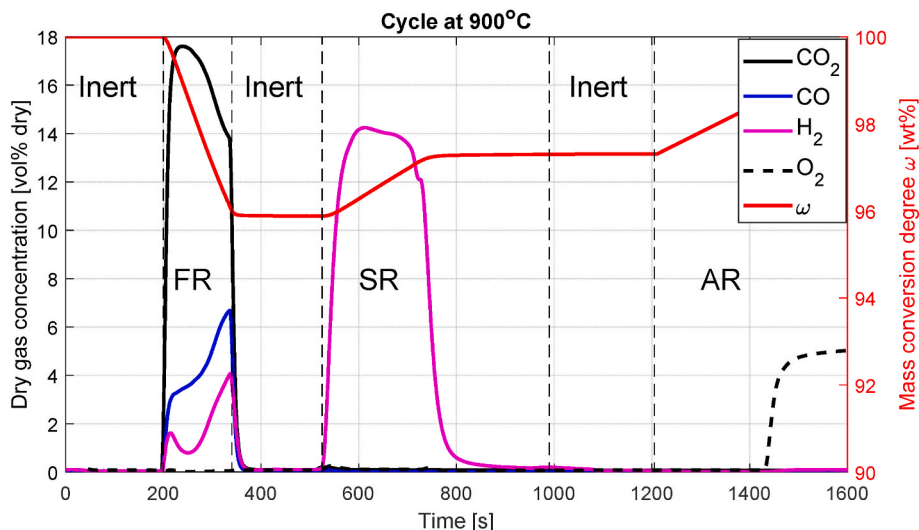


Fig. 5. Dry gas concentration profiles during one cycle with 15 g MAF conducted at 900 °C including reduction (FR), steam oxidation (SR), and oxidation (AR). The change in mass conversion degree (ω) is presented in the secondary y-axis.

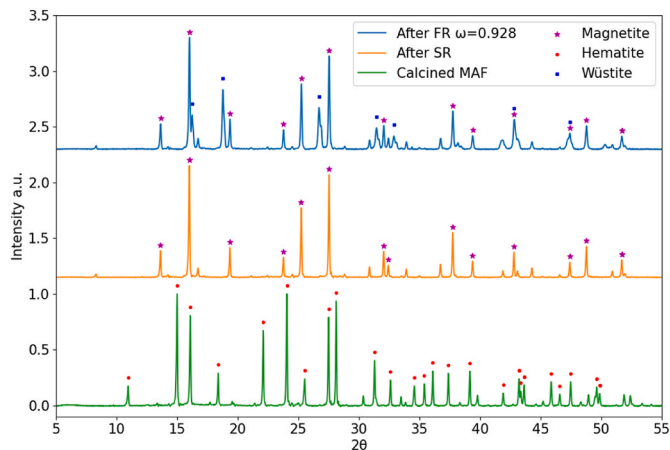


Fig. 6. XRD diffractogram of the three MAF samples: calcined MAF ($\omega = 1$), MAF extracted after reduction at 900 °C (FR) ($\omega = 0.928$) and MAF after steam oxidation at 900 °C (SR) ($\omega = 0.967$). Data was collected with MoK_α radiation ($\lambda = 0.7093 \text{ \AA}$).

defluidization was observed during the oxidation step. Despite this, an additional reduction step was performed to investigate the reactivity, as illustrated by the dashed lines, which show a reduction in reactivity as well as a linear decrease as a function of mass conversion degree.

After defluidization, particles were analyzed by SEM-EDX, and the results are shown in Fig. A.2. The analysis reveals particles with less porous surface, due to sintering. Furthermore, studying the cross-section of the sample showed sintered particles. Thus, defluidization was observed after oxidation following deep reduction of MAF and attributed to thermal sintering. Thermal sintering could also occur without defluidization of the bed but cause a decreased reactivity by clogging pores at the particle surface and thereby limiting the gas-solid-contact.

3.4.1. Apparent kinetics during reduction

Understanding the apparent kinetics is essential for designing and optimizing the performance of MAF for hydrogen production. The rate at which CO and H₂ are converted influences the overall efficiency and yield of the system. Therefore, it is crucial to investigate the apparent rate constants for CO and H₂ as functions of the extent of reaction, i.e. the mass conversion degree, as well as temperature.

The apparent rate constants for CO and H₂, as a function of the mass conversion degree and temperature, are presented in Fig. 8 using syngas as fuel. The mass-based rate constants were derived from equations (19) and (22). It is evident that the rate constants are largely dependent on both the mass conversion degree and temperature. As the mass conversion degree increases, the rate constant for CO and H₂ show a clear increase, indicating that reactivity improves at higher degrees of oxidation. Additionally, higher temperatures result in higher rate constants and thereby faster reactions, as expected. The rate of conversion as a function of the mass conversion degree is shown in Fig. A.3.

A correlation with the crystalline phases can also be identified. For example, there is a change in the slope of the curves occurring at $\omega = 0.967$, indicating a change in reduction from Fe₂O₃–Fe₃O₄ to Fe₃O₄–FeO. The rate constants decrease as hematite is depleted, meaning that the reduction progresses slower for the reduction to wüstite. Furthermore, it is observed that the rate constant for H₂ consistently exceeds that of CO indicating that the reactivity towards H₂ is higher. These findings emphasize the important influence of the mass conversion degree on the reactivity of iron oxides.

To the best of our knowledge, there are no apparent kinetic data derived from fluidized bed experiments for iron-based oxygen carrier materials below the mass conversion degree 0.97 and this is the first study to report kinetic data for iron-based materials at high reduction degrees. Thus, the mass-based rate constants presented in Fig. 9 were further compared with the literature which provides the constants only for the mass conversion degree of 0.97 for the iron-based oxygen carrier ilmenite derived under similar fluidized bed experiments [30]. The apparent rate constant $k_{F,CO}$ for MAF 950 °C, is almost twice as high ($5.9 \cdot 10^{-3} \text{ m}^3 \text{ kg}^{-1} \text{ s}^{-1}$) as that of ilmenite ($3.0 \cdot 10^{-3} \text{ m}^3 \text{ kg}^{-1} \text{ s}^{-1}$). The rate constant for hydrogen shows a similar trend where $10.3 \cdot 10^{-3} \text{ m}^3 \text{ kg}^{-1} \text{ s}^{-1}$ for MAF, is higher compared to ilmenite $4.5 \cdot 10^{-3} \text{ m}^3 \text{ kg}^{-1} \text{ s}^{-1}$.

The apparent rate constants from Fig. 8 were utilized to calculate the activation energies. The activation energies for CO and H₂, as a function of the mass conversion degree, is shown in Fig. 9. For CO, the activation energy varies from 32.7 to 70.5 kJ/mol and for H₂ between 22.6 and 67.4 kJ/mol. These values are in the range of the reported activation energies for reduction to wüstite, as obtained from micro fluidized bed experiments [15]. Furthermore, the activation energy for H₂ is always lower than for CO, and the difference becomes less pronounced at lower mass conversion degrees. This implies that H₂ is more reactive as a reducing agent.

The apparent activation energy values presented in Fig. 9 provide valuable insights into the probable rate-controlling mechanisms during

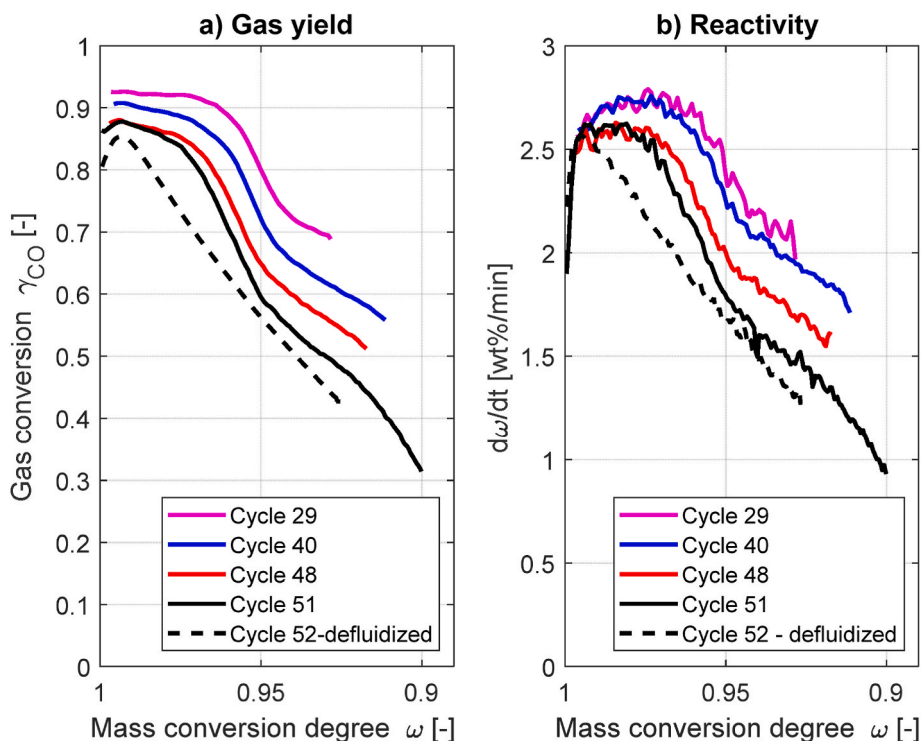


Fig. 7. Influence of cycling on the (a) gas yield, and (b) rate of conversion as a function of the mass conversion degree (ω) with 15 g of MAF and CO as fuel at 900 °C.

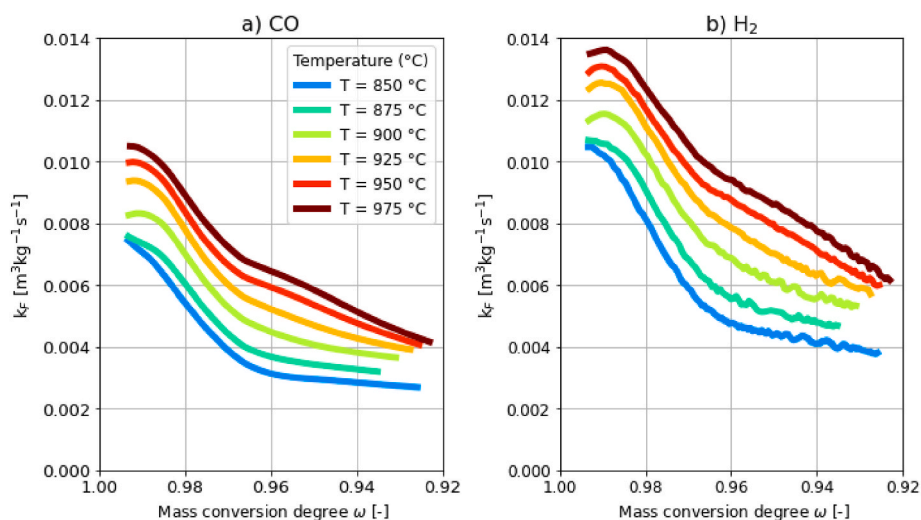


Fig. 8. Apparent rate constant k_F for the two gaseous components (a) CO and (b) H_2 for temperatures between 850 °C and 975 °C, as a function of the mass conversion degree (ω) with 2.5 g MAF and syngas as fuel.

the reduction and oxidation of iron oxides. At the initial stage of the reduction, ω from 1 to 0.967, there is a clear increasing trend in the activation energy for both CO and H_2 . This trend suggests a transition in the rate-controlling mechanism. In the early stages, the reducing gas reacts directly with the exposed hematite surface, where gas diffusion is relatively unhindered, resulting in low apparent activation energies. However, as the reduction progresses, a product layer of magnetite forms. This magnetite layer created a physical barrier that limits the access of reactant gases to the unreacted core, increasing the resistance. This leads to a reduction in the reaction rate, and an increase in the apparent activation energy. Accordingly, the system transitions from a diffusion-limited regime to one where surface reaction kinetics dominate. As a result, the rate of reduction becomes more dependent on the

interfacial microstructure.

A peak in activation energy was observed at $\omega \sim 0.967$, marking the transition from the reduction of hematite to magnetite, to the reduction from magnetite to wüstite. Following this peak, a notable decrease in the activation energy occurs, which aligns with the initiation of the magnetite-to-wüstite reduction step. Previous research [35] show that reduction of magnetite results in a porous structure and is accompanied by enhanced reaction rates due to lower diffusion resistance. Hence, the phase change for ω below 0.967 is accompanied by the formation of a more porous product layer, which introduces vacancies and interstitial sites in the crystal lattice. These structural changes and defects promote a more porous structure which allows for easier gas diffusion. As a result, the reduction becomes partially controlled again by gas-phase transport,

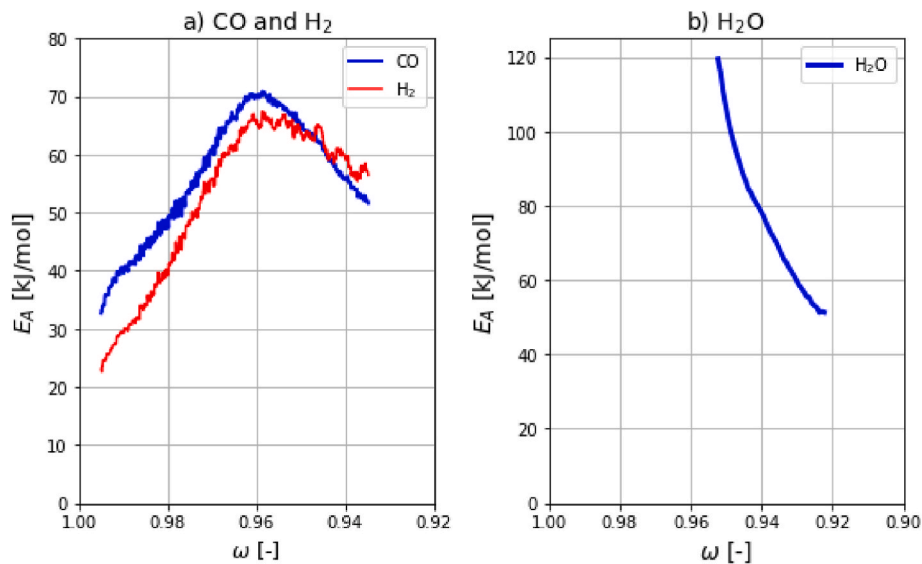


Fig. 9. The activation energy (E_a) as a function of the mass conversion degree ω . For a) the reduction of MAF with CO and H₂, and b) oxidation of MAF with steam.

as indicated by the lower activation energy. This interpretation aligns with the typical activation energy ranges: gas diffusion (8–16 kJ/mol), combined gas diffusion and interfacial chemical reaction (29–42 kJ/mol), interfacial chemical reaction (60–67 kJ/mol), and solid-state diffusion (>90 kJ/mol) [34,36].

The apparent activation energy for oxidation and reduction of iron oxides is influenced by the interplay between phase transformations, product layer morphology and gas diffusion mechanisms. This emphasizes the important role of microstructural evolution and phase behavior in determining the apparent kinetics. While the trends in activation energy and proposed shift in the rate-controlling mechanisms offer valuable insights, they are based on the apparent kinetic parameters derived from experimental data. To definitively identify the mechanisms involved, complementary studies are necessary to provide a deeper understanding of the structural and morphological changes occurring during the oxidation and reduction processes. However, such studies are beyond the scope of the current work, and future investigations are necessary to further validate the proposed mechanisms.

To the best of our knowledge, this is the first study to present experimentally derived apparent activation energies for this specific system—magnetite fines (MAF), relevant fuel gases, and varying degrees of reduction—providing novel insights into how the apparent kinetics evolve throughout the redox cycles. The findings therefore represent a

logical and necessary step forward in understanding the reactivity of this material under realistic operating conditions and form a foundation for future studies targeting more detailed mechanistic understanding.

3.5. Optimizing hydrogen production

The effect of temperature and the influence of the reduction level of MAF on hydrogen production via chemical looping hydrogen production process was investigated in detail. The rate of conversion ($d\omega/dt$) during steam oxidation is presented in Fig. 10a for temperatures between 600 °C and 900 °C. The figure illustrates that the maximum rate of conversion occurs around 800 °C. The rate increases as the temperature rises from 600 °C to 800 °C, but decreases above 800 °C. According to thermodynamic equilibrium, see Fig. 2, higher H₂-yields are favored by lower temperatures. The theoretical limit for achieving 100 % conversion to magnetite (Fe₃O₄) is at $\omega = 0.967$. Temperatures above 800 °C enable complete oxidation of the sample, whereas temperatures below 800 °C exhibit a lower rate of conversion and do not reach complete oxidation. This is attributed to the oxygen mobility within particles, which decreases with lower temperatures.

The results here imply that temperatures around 800 °C are optimal for achieving a high reaction rate and production of hydrogen in the steam reactor. This is further supported by the data presented in Table 6,

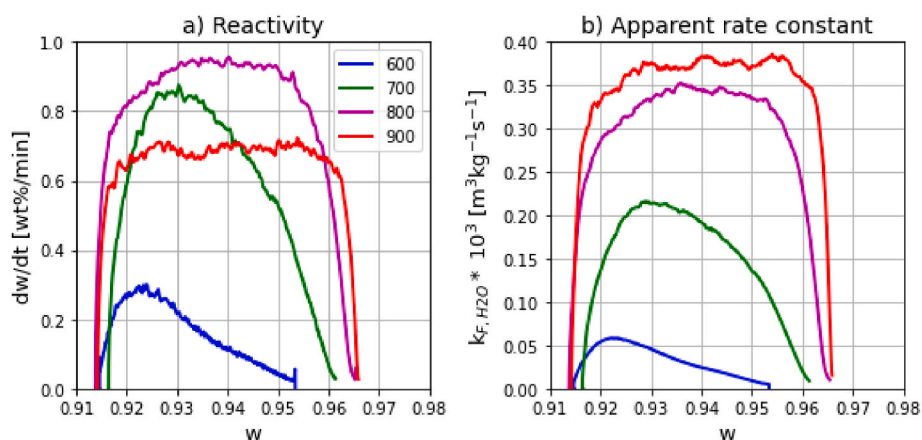


Fig. 10. The a) rate of reaction, and b) apparent rate constant k_{F,H_2O} for temperatures between 600 °C and 900 °C as a function of the mass conversion degree (ω) for the oxidation of MAF with H₂O.

Table 6

Hydrogen production rate ($\text{mmol g}^{-1} \text{s}^{-1}$) as functions of temperature after reduction to $\omega = 0.915$.

Temperature	600 °C	700 °C	800 °C	900 °C
$\text{mmol g}^{-1} \text{min}^{-1}$	0.11	0.23	0.37	0.34

which shows the hydrogen production rate ($\text{mmol g}^{-1} \text{s}^{-1}$). As shown in the table, the hydrogen production rate is the highest for 800 °C.

The production of hydrogen is highly dependent on the reduction level achieved in the FR. To investigate this, different reduction times, corresponding to varying ω -values were tested, and the steam oxidation of MAF was allowed to continue until the outlet concentration of

hydrogen dropped below 0.2 vol%. A summary of all experiments, showing the production as a function of the mass conversion degree is presented in Fig. A.4a. The figure demonstrates the linear increase in hydrogen production as a function of ω . In the figure, there are two outliers located near $\omega = 0.9$. The reaction rate, presented in Fig. A.4b, shows that the reaction rate remains constant for mass conversion degrees in the range from 0.97 to 0.91 but increases rapidly below 0.91. In this region, reduction to metallic iron likely occurs, and the subsequent increase in hydrogen production and reaction rate can be attributed to the oxidation of metallic iron. After the formation of metallic iron, a decrease in reactivity is observed due to sintering, and defluidization was observed during the following air oxidation step.

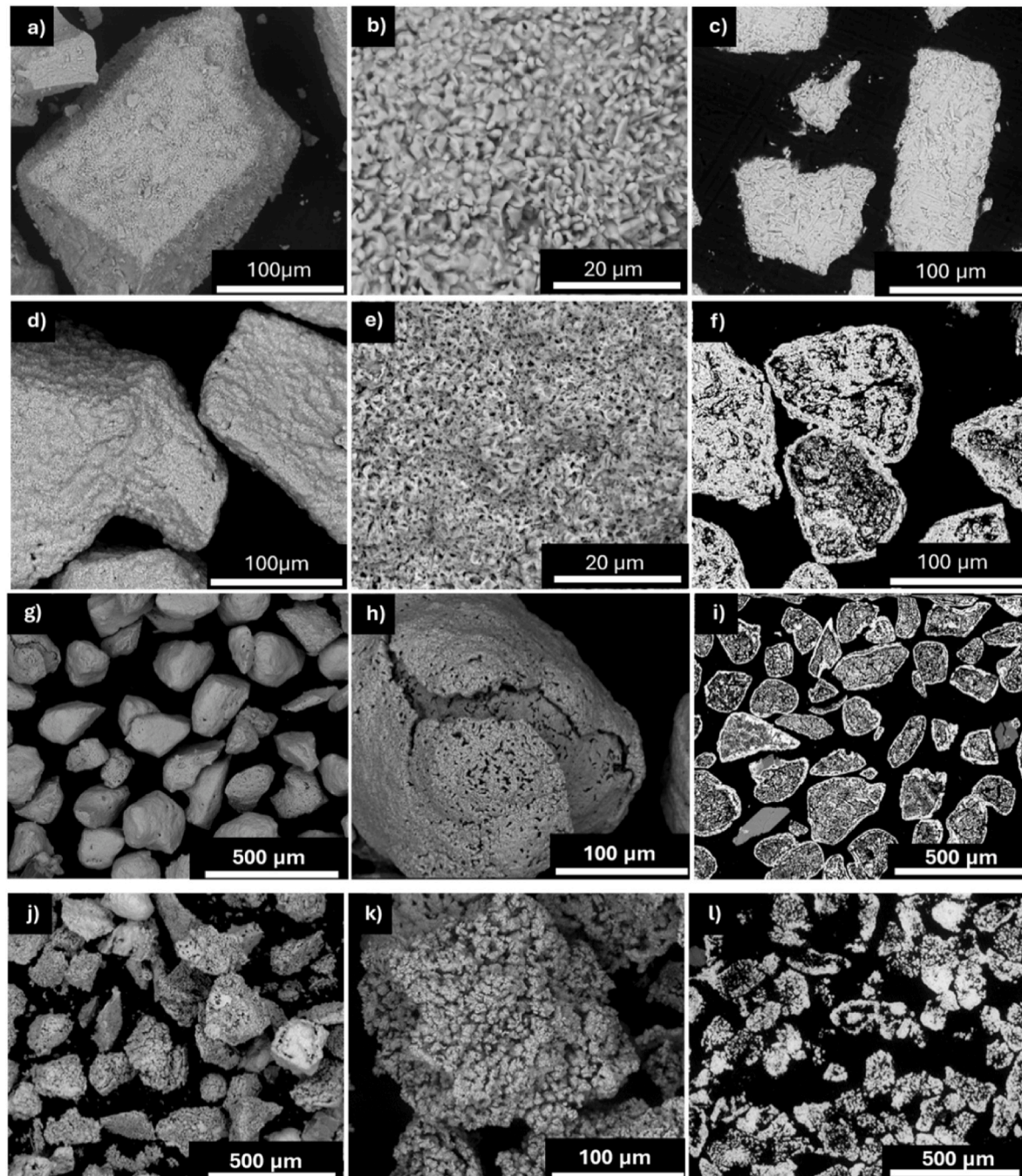


Fig. 11. Micrographs showing the sample topology (left and middle columns) and cross-sections (right column) of the material at different stages. (a–c) Calcined unused MAF, MAF extracted after (d–f) activation, (g–i) 26 cycles, and (j–l) 52 cycles after defluidization.

3.5.1. Apparent kinetics during hydrogen production

The apparent rate constant for oxidation of MAF with H₂O as a function of the mass conversion degree and temperature is presented in Fig. 10b. The mass-based rate constants were obtained by equation (19). It is evident from Fig. 10b that the rate constant increases with temperature showing that the proposed model successfully captures the influence of the thermodynamic driving force, which plays an important role for steam oxidation of iron and iron oxides. For ω between 0.92 and 0.967, the apparent rate constant remains around 0.00035 and 0.00037 m³kg⁻¹s⁻¹ for 800 °C and 900 °C, respectively. Below 800 °C, a decrease in the apparent rate constant is observed with decreasing temperature and increasing ω . Compared to the reduction step, the rate constant for steam oxidation is approximately 10 times lower.

The activation energy was determined for ω between 0.92 (to avoid the fluctuations at the start of oxidation) and 0.953 (where data for 600 °C ends). The activation energy during steam oxidation is illustrated in Fig. 9b, showing that it varies between 51.2 and 121.3 kJ/mol. These values are comparable to reported values in literature (47–77.9 kJ/mol) derived from oxidation experiments of iron oxides [24,25]. However, it is evident that at more oxidized states of the material, oxidation is primarily controlled by solid-state diffusion, as indicated by the high activation energy values (>90 kJ/mol). Hence, at low temperatures, the reduction rate is hindered by the diffusion of oxygen within the solid structure explaining why complete oxidation to magnetite was not achieved at lower temperatures.

3.6. Evolution of particle morphology

During continuous cycling between oxidation and reduction phases, particles undergo structural and topological changes. To illustrate changes in morphology, the unused and calcined sample is compared to samples extracted at three different stages – after 10 cycles, 26 cycles, and after defluidization (52 cycles).

Micrographs of unused MAF and MAF after activation are presented in Fig. 11a–c and d–f, respectively. A smoother surface can be observed for the unused calcined sample (Fig. 11b) compared to the activated one (Fig. 11b). In addition to changes occurring on the surface, there are also significant structural changes occurring within the particles, as seen in Fig. 11c–f and i. The changes in particle morphology are closely related to the performance. To exemplify, the reactivity increases during activation, as illustrated in Fig. 4. During these first cycles, pores are developed on the surface and inside the particles which enhances the gas-solid contact and thereby increases the reaction rate.

After activation, an iron oxide layer can be observed on the surface of the particles, see Fig. 11f. The iron oxide layer becomes more pronounced with an increasing number of cycles. For example, particles extracted after 26 cycles show the presence of a double iron layer on the surface (Fig. 11i). Continuous cycling between oxidation and reduction promotes the development of pores, as seen after 26 and 53 cycles in Fig. 11h and k, respectively. Compared to the activated sample, some particles also exhibit cracks in the outer surface and peeling of the outer layer (Fig. 11h), which allows a second iron layer to form beneath the first one.

Furthermore, it is observed that particles develop voids internally (Fig. 11f) and with time, some particles even become hollow (Fig. 11l). The internal voids and external pore development, likely occur due to iron atoms moving in the crystalline structure due to changes in the oxygen partial pressure. Hence, vacancies are left behind which coalesce into voids. Iron diffusion occurs on preferred sites, which can be seen as veins in the sample (Fig. 11d). Because these pathways are uneven, likely due to grain boundaries, the formed iron layer becomes less adherent with time and is more prone to cracks upon changes in surrounding conditions (including temperature, pressure and gas atmosphere). The cracking of the iron layer makes the material prone to disintegrate, which is observed as fines in Fig. 11l.

When the bed was reduced to $\omega = 0.899$ at 900 °C, defluidization

occurred during the subsequent AR-step. This is attributed to the highly exothermic oxidation, which causes a temperature increase in the bed. After deep reduction, a temperature increase of 37 °C was measured during oxidation with air. Consequently, even higher localized temperatures could occur, potentially leading to defluidization due to sintering. Micrographs of particles after defluidization are presented in Fig. A.2a, showing sintering in the form of smooth and nonporous particle surfaces. The cross-section of the same sample is shown in Fig. A.2b, clearly illustrating sintered particles. It is further important to address the fact that at larger scales, fluidization velocities will be higher, and heat will be extracted during the oxidation step which would lower the risks of sintering. Furthermore, defluidization was not observed during oxidation with steam, as the reaction is significantly less exothermic compared to oxidation with air, which is approximately ten times more exothermic. As a result, fluidization remained stable when the reduction step was followed by steam oxidation rather than direct oxidation with air which is an advantage for implementing MAF in chemical looping water splitting.

4. Conclusion

This study investigates the potential of magnetite fines (MAF) as an oxygen carrier for continuous hydrogen production. MAF, a widely available intermediate product in the European iron and steel industry, was utilized in a fluidized bed reactor to generate hydrogen via water splitting, using low-grade gaseous fuels as reducing agents. Furthermore, the process enables the production of CO₂ in a form suitable for carbon capture and storage under optimized reactor configurations. The promising results make this process an interesting option for the European steel industry to achieve fossil-free steel production.

A kinetic model was developed to examine the gas-solid reaction kinetics in fluidized beds. The model accounts for thermodynamic limitations, which are particularly important for the steam-iron reaction, but could also be applied to other systems. The kinetic model was applied to examine MAF's reactivity during reduction with CO and H₂, as well as oxidation with H₂O.

The results show a significant dependence of reactivity on both temperature and the mass conversion degree. The reactivity increased with temperature and over the initial ten reduction-oxidation cycles and decreased when the mass conversion degree fell below 0.967. The apparent activation energy varied with the extent of conversion: for CO reduction, it ranged from 32.7 to 70.5 kJ/mol; for H₂ reduction, from 22.6 to 67.4 kJ/mol. During steam oxidation, activation energy progressively increased from 51.2 to 121.3 kJ/mol, reflecting a change in the rate-controlling step as the reaction proceeds. These variations imply that the rate-controlling mechanisms may change with the progression of the reduction.

Changes in reactivity are also linked to microstructural evolution. Increased porosity during the initial cycles enhanced the reaction rate, whereas deeper reduction led to sintering and reduced performance. Thus, to maintain high reactivity, operation should be maintained within a range that avoids complete reduction to metallic iron. The highest observed hydrogen production rate was 0.37 mmol g⁻¹ min⁻¹ at 800 °C. Overall, the results demonstrate the feasibility of continuous hydrogen production using MAF as an oxygen carrier.

CRedit authorship contribution statement

Ivana Staničić: Writing – original draft, Methodology, Investigation. **Robin Faust:** Writing – review & editing, Investigation. **Pavleta Knutsson:** Writing – review & editing, Supervision. **Victor Purnomo:** Writing – review & editing. **Henrik Leion:** Writing – review & editing. **Tobias Mattisson:** Writing – review & editing, Methodology. **Magnus Rydén:** Writing – review & editing, Project administration, Funding acquisition.

Notes

The authors declare no competing financial interest.

Declaration of competing interest

The authors declare that they have no known competing financial interests or personal relationships that could have appeared to influence the work reported in this paper.

Acknowledgment

This work has been supported by the Swedish Energy Agency project P2022-00544 - Production of hydrogen and biochar from wood fuels with a new process that utilizes the steam-iron reaction and iron ore concentrate and by Chalmers Area of Advance Energy. A part of this work was conducted as a student project at Chalmers involving Alexander Klute, Ellen Sjöstrand, Adrian Christiansen, Jacob Linnarsson, Lina Landgren, and Niloofar Bastegani.

Appendix A. Supplementary data

Supplementary data to this article can be found online at <https://doi.org/10.1016/j.ijhydene.2025.05.223>.

References

- [1] Kountouris I, Bramstoft R, Madsen T, Gea-Bermúdez J, Münster M, Keles D. A unified European hydrogen infrastructure planning to support the rapid scale-up of hydrogen production. *Nat Commun* 2024;06/29 2024;15(1):5517. <https://doi.org/10.1038/s41467-024-49867-w>.
- [2] I. E. Agency. "Hydrogen Patents for a Clean Energy Future." International Energy Agency. <https://www.iea.org/reports/hydrogen-patents-for-a-clean-energy-future> (accessed).
- [3] Messerschmitt A. Process for producing hydrogen. U.S. Patent 1910:971206.
- [4] Voitic G, Hacker V. Recent advancements in chemical looping water splitting for the production of hydrogen. *RSC Adv* 2016;6(100):98267–96. <https://doi.org/10.1039/C6RA21180A>.
- [5] Tarman PB, Biljetina R. Steam-iron process for hydrogen production. Presented at the conference: 85th national meeting of the American institute of chemical engineers, Philadelphia, PA, USA, 4 jun 1978, United States. 1978 [Online]. Available: <https://www.osti.gov/biblio/5288162>.
- [6] Gasior SJ, Forney AJ, Field JH, Bienstock D, Benson HE. Production of synthesis gas and hydrogen by the steam–iron process. Pilot-plant study of fluidized and free-falling beds. United States Bureau of Mines, Report of Investigations; 1961.
- [7] Rydén M, Arjmand M. Continuous hydrogen production via the steam-iron reaction by chemical looping in a circulating fluidized-bed reactor. *Int J Hydrogen Energy* 2012;37(6):4843–54. <https://doi.org/10.1016/j.ijhydene.2011.12.037>.
- [8] Bohn CD, et al. Production of very pure hydrogen with simultaneous capture of carbon dioxide using the redox reactions of iron oxides in packed beds. *Ind Eng Chem Res* 2008;10/15 2008;47(20):7623–30. <https://doi.org/10.1021/ie800335j>.
- [9] Gupta P, Velazquez-Vargas LG, Fan L-S. Syngas redox (SGR) process to produce hydrogen from coal derived syngas. *Energy Fuels* 2007;09/01 2007;21(5):2900–8. <https://doi.org/10.1021/ef060512k>.
- [10] Nemati N, Filiu Moreno P, Rydén M. Investigation of the hydrodynamics of packed-fluidized beds: characterization of solids flux. *Fuel* 2023;03/01/2023;335:127010. <https://doi.org/10.1016/j.fuel.2022.127010>.
- [11] Bale CW, et al. "FactSage thermochemical software and databases - 2010 - 2016," *Calphad* 2016;54:35–53 [Online]. Available: www.factsage.com.
- [12] Chang W, et al. Recent advances of oxygen carriers for hydrogen production via chemical looping water-splitting. *Catalysts* 2023;13(2):279 [Online]. Available: <https://www.mdpi.com/2073-4344/13/2/279>.
- [13] Zeng D, et al. Ternary mixed spinel oxides as oxygen carriers for chemical looping hydrogen production operating at 550 °C. *ACS Appl Mater Interfaces* 2019/11/27 2019;11(47):44223–32. <https://doi.org/10.1021/acsami.9b14989>.
- [14] Dilmac N, Yoruk S, Gulaboglu SM. Investigation of direct reduction mechanism of ateppe iron ore by hydrogen in a fluidized bed. *Metall Mater Trans B* 2015/10/01 2015;46(5):2278–87. <https://doi.org/10.1007/s11663-015-0409-8>.
- [15] Chen H, Zheng Z, Chen Z, Bi XT. Reduction of hematite (Fe₂O₃) to metallic iron (Fe) by CO in a micro fluidized bed reaction analyzer: a multistep kinetics study. *Powder Technol* 2017/07/01/2017;316:410–20. <https://doi.org/10.1016/j.powtec.2017.02.067>.
- [16] Chen H, Zheng Z, Shi W. Investigation on the kinetics of iron ore fines reduction by CO in a micro-fluidized bed. *Procedia Eng* 2015/01/01/2015;102:1726–35. <https://doi.org/10.1016/j.proeng.2015.01.308>.
- [17] Zhang T, Lei C, Zhu Q. Reduction of fine iron ore via a two-step fluidized bed direct reduction process. *Powder Technol* 2014/03/01/2014;254:1–11. <https://doi.org/10.1016/j.powtec.2014.01.004>.
- [18] Zhang J, Li S, Wang L. Kinetics analysis of direct reduction of iron ore by hydrogen in fluidized bed based on response surface methodology. *Int J Hydrogen Energy* 2024/01/02/2024;49:1318–31. <https://doi.org/10.1016/j.ijhydene.2023.09.243>.
- [19] Li P, Yu J, Li Y, Gao P, Han Y. New approach to reduce carbon emissions by hydrogen reduction of boron-bearing iron concentrate in a fluidized bed: reduction kinetics and microstructure analysis. *Miner Eng* 2024/07/15/2024;212:108727. <https://doi.org/10.1016/j.mineng.2024.108727>.
- [20] Cheng Y, Shen Z, Liang Q, Dai Z, Liu H. Reduction kinetics of non-spherical hematite particle in CO atmosphere with multi-step limited reaction zone modification. *Metall Mater Trans B* 2024/11/19 2024. <https://doi.org/10.1007/s11663-024-03371-0>.
- [21] El-Geassy AA. Gaseous reduction of Fe₂O₃ compacts at 600 to 1050 °C. *JMatS* 1986/11/01 1986;21(11):3889–900. <https://doi.org/10.1007/BF02431626>.
- [22] Cerciello F, et al. Kinetics of iron reduction upon reduction/oxidation cycles. *Int J Hydrogen Energy* 2024/05/02/2024;65:337–47. <https://doi.org/10.1016/j.ijhydene.2024.04.008>.
- [23] Cabello A, Zornoza B, Mendiara T, Abad A, de Diego LF. Versatile low cost oxygen carrier for chemical looping processes requiring different degree of iron oxide reduction. *Energy Fuels* 2024/11/07 2024;38(21):20707–20. <https://doi.org/10.1021/acs.energyfuels.4c02906>.
- [24] Stehle RC, Bobek MM, Hooper R, Hahn DW. Oxidation reaction kinetics for the steam-iron process in support of hydrogen production. *Int J Hydrogen Energy* 2011/11/01/2011;36(23):15125–35. <https://doi.org/10.1016/j.ijhydene.2011.08.074>.
- [25] Go KS, Son SR, Kim SD. Reaction kinetics of reduction and oxidation of metal oxides for hydrogen production. *Int J Hydrogen Energy* 2008/11/01/2008;33(21):5986–95. <https://doi.org/10.1016/j.ijhydene.2008.05.039>.
- [26] Zhang X, Yip ACK, Pang S. Advances in the application of active metal-based sorbents and oxygen carriers in chemical looping biomass steam gasification for H₂ production. *Int J Hydrogen Energy* 2023/04/01/2023;48(28):10394–422. <https://doi.org/10.1016/j.ijhydene.2022.11.317>.
- [27] Guo L, Bao Q, Gao J, Zhu Q, Guo Z. A review on prevention of sticking during fluidized bed reduction of fine iron ore. *ISIJ Int* 2020;60(1):1–17. <https://doi.org/10.2355/isijinternational.ISIJINT-2019-392>.
- [28] Störner F, Staničić I, Knutsson P, Mattisson T, Rydén M. Potassium interactions with copper slag and magnetite fines in chemical-looping processes. *Fuel Process Technol* 2025/06/01/2025;270:108192. <https://doi.org/10.1016/j.fuproc.2025.108192>.
- [29] Wen CY, Yu YH. A generalized method for predicting the minimum fluidization velocity. *AIChE J* 1966;12(3):610–2. <https://doi.org/10.1002/aic.690120343>.
- [30] Mei D, Soleimanisalam AH, Lyngfelt A, Leion H, Linderholm C, Mattisson T. Modelling of gas conversion with an analytical reactor model for biomass chemical looping combustion (bio-CLC) of solid fuels. *Chem Eng J* 2022/04/01/2022;433:133563. <https://doi.org/10.1016/j.cej.2021.133563>.
- [31] Markström P, Linderholm C, Lyngfelt A. Analytical model of gas conversion in a 100kW chemical-looping combustor for solid fuels—comparison with operational results. *Chem Eng Sci* 2013/06/07/2013;96:131–41. <https://doi.org/10.1016/j.ces.2013.04.001>.
- [32] Strangway PK. Kinetics of reduction of iron oxide by re-formed natural gas. *Metallurgy and materials science*. Toronto University; 1986.
- [33] Hammam A, et al. Isothermal and non-isothermal reduction behaviors of iron ore compacts in pure hydrogen atmosphere and kinetic analysis. *Mining, Metallurgy & Exploration* 2021/02/01 2021;38(1):81–93. <https://doi.org/10.1007/s42461-020-00317-3>.
- [34] Xudong M, Xiaojun H, Yuewen F, Kuochih C. "Effect of water vapor on the reduction kinetics of hematite powder by hydrogen-water vapor in different stages." *J Min Metall B Metall* 2023;59(1):65–76. <https://doi.org/10.2298/JMMB220523006M> (in English).
- [35] Matthew SP, Cho TR, Hayes PC. Mechanisms of porous iron growth on wustite and magnetite during gaseous reduction. *Metall Trans A B* 1990/08/01 1990;21(4):733–41. <https://doi.org/10.1007/BF02654252>.
- [36] Nasr MI, Omar AA, Khedr MH, El-Geassy AA. Effect of nickel oxide doping on the kinetics and mechanism of iron oxide reduction. *ISIJ Int* 1995;35(9):1043–9. <https://doi.org/10.2355/isijinternational.35.1043>.